

UC Berkeley

UC Berkeley Previously Published Works

Title

Polarization dependent photoemission as a probe of the magnetic ground state in the van der Waals ferromagnet VI3

Permalink

<https://escholarship.org/uc/item/8cp652wj>

Journal

Applied Physics Letters, 121(18)

ISSN

0003-6951

Authors

Bergner, Derek
Kong, Tai
Ai, Ping
[et al.](#)

Publication Date

2022-10-31

DOI

10.1063/5.0108498

Copyright Information

This work is made available under the terms of a Creative Commons Attribution License, available at <https://creativecommons.org/licenses/by/4.0/>

Peer reviewed

Polarization dependent photoemission as a probe of the magnetic ground state in the layered ferromagnet VI_3

Derek Bergner,¹ Tai Kong,^{2, a)} Ping Ai,^{3,4} Daniel Eilbott,^{3,4} Claudia Fatuzzo,^{3,4} Samuel Ciocys,^{3,4} Nicholas Dale,^{3,4} Conrad Stansbury,^{3,4} Drew Latzke,^{3,4} Everardo Molina,¹ Ryan Reno,¹ Robert J. Cava,² Alessandra Lanzara,^{3,4} and Claudia Ojeda-Aristizabal¹

¹⁾*Department of Physics and Astronomy, California State University Long Beach, Long Beach, California 90840, USA*

²⁾*Department of Chemistry, Princeton University, Princeton, New Jersey, 08544, USA*

³⁾*Department of Physics, University of California Berkeley, California 94720, USA*

⁴⁾*Materials Sciences Division, Lawrence Berkeley National Laboratory, Berkeley, California 94720, United States*

(Dated: 16 June 2022)

Layered ferromagnets are thrilling materials from both a fundamental and technological point of view. VI_3 is an interesting example, with a complex magnetism that differentiates it from the first reported Cr based layered ferromagnets. Here, we show in an indirect way through Angle Resolved Photoemission Spectroscopy (ARPES) experiments, the importance of spin-orbit coupling setting the electronic properties of this material. Our light polarized photoemission measurements point to a ground state with a half-filled e'_\pm doublet, where a gap opening is triggered by spin-orbit coupling enhanced by electronic correlations.

^{a)}Current affiliation: Department of Physics, University of Arizona, Tucson Arizona, 85721, USA

Layered ferromagnets, van der Waals materials that exhibit a magnetic order at the level of single layer, bring a new functionality to the family of 2-dimensional crystals, opening the door to ultrathin spintronic applications. Vanadium(III) iodide (VI_3) is a van der Waals (vdW) Mott insulator made of honeycomb vanadium layers separated by an iodine-iodine vdW gap with the remarkable property of intrinsic ferromagnetism. Despite the fact that VI_3 has proved to be extremely sensitive to air, its recently reported unusual thickness-dependent magnetism with an increase of the Curie temperature as the layer number decreases¹, makes it a compelling platform for the engineering of magnetism in electronic devices. Angle Resolved Photoemission Spectroscopy (ARPES) is an excellent tool to study the electronic properties of layered materials. Its ultrahigh vacuum environment and in-situ cleaving capability reduces the limitations and challenges associated to probing air-sensitive materials.

VI_3 's electronic properties derive from a combination of crystal field effects, electronic correlations and spin-orbit coupling. In VI_3 , vanadium ions (V) are surrounded by I_6 octahedra which provides a crystal field that splits the five-fold degenerate V-d orbitals into a lower triplet t_{2g} and an upper doublet e_g . Additional trigonal distortions caused by the elongation of VI_6 octahedra along one of the [111] axes², causes an additional split of the t_{2g} levels into a singlet a_{1g} and a doublet e'_{\pm} (see Figure 1). $|a_{1g}\rangle$ has a simple form in coordinates where the z axis aligns with the trigonal distortion, and x and y axes are in the perpendicular plane, pointing along the z-direction. The other two t_{2g} orbitals $|e'_{\pm}\rangle$ are complex and have the shape of a torus^{2,3}.

There is not yet consensus on what is the exact mechanism responsible of the observed bandgap in VI_3 . The two V d^2 electrons in VI_3 may occupy the $|a_{1g}\rangle$ and $|e'_{\pm}\rangle$ orbitals into the state $e_{\pm}^2 a_{1g}^0$, that together with electronic correlations leads to a Mott insulator³⁻⁵, or electrons may partially fill the $|e'_{\pm}\rangle$ orbitals, which leads in principle to a metallic ground state $a_{1g}^1 e_{\pm}^1$; however spin-orbit coupling is capable of splitting the half filled $|e'_{\pm}\rangle$, that in conjunction with electronic correlations leads also to a Mott insulator^{5,6}. Both scenarios have been proved possible through first principle calculations, and are consistent with the known $S=1$ state for VI_3 ^{5,6}.

Understanding the t_{2g} orbitals in VI_3 is fundamental, as they not only set the insulating character of this vdW material but also determine its magnetic properties. Perpendicular magnetic anisotropy, that refers to the preferred orientation of magnetic vectors perpendicular to the layer plane, is a fundamental characteristic in magnetic materials for appli-

cations, and most importantly, it is essential for the existence of magnetic order at low dimensions⁷. Perpendicular magnetic anisotropy comes from a microscopic effect, called single ion anisotropy or magnetocrystalline anisotropy, caused by the orbital momentum along the normal of the bonding plane quenching due to crystalline fields. The first layered ferromagnets reported in the literature were Cr based^{8,9}, such as CrI₃, where crystal field effects also split the 5-fold degenerate Cr-d orbitals into t_{2g} and e_g states however, the degeneracy of the t_{2g} orbital for Cr d³ is unlifted and yields no magnetocrystalline anisotropy. Perpendicular magnetic anisotropy in CrI₃ comes rather from the weak exchange anisotropy brought by the heavy I 5p orbitals and their hybridization with Cr 3d orbitals^{6,10,11}. VI₃ has a large magnetocrystalline anisotropy (one order of magnitude larger than for CrI₃) that together with spin-orbit coupling, is responsible for the observed perpendicular magnetic anisotropy. In VI₃, it is spin-orbit coupling that aligns the magnetic moment of the V ions along the z-axis via the strong magnetocrystalline anisotropy and produces the observed perpendicular magnetic anisotropy⁶. Angle-dependent magnetization measurements have demonstrated that the magnetic moment in VI₃ is in fact canted by $\approx 40^\circ$ from the normal to the ab plane in a wide temperature range (10 K - 60 K), within the range of the two ferromagnetic phases reported for VI₃ as well as its structural phase transition. The observed magnetization canted easy-axis differentiates VI₃ from the Ising-type magnetism reported for CrI₃¹².

The orientation of the V 3d orbitals that host the magnetic Mott ground state, discernible through the use of different light polarizations in ARPES, can give insight on the ground state that brings magnetism to this vdW material. Previous photoemission experiments have characterized the valence band structure of bulk VI₃¹³ however, further understanding of the character of the observed band manifolds remains elusive. Here we report a deep study on the linear and circular dichroism of VI₃ photoemission, that together with the effects of light energy and alkaline doping brings insight on the orbitals' properties that play an important role in 2-dimensional magnetism.

VI₃ millimeter-sized single crystals were synthesized by a chemical vapor transport method as reported in 14. A stoichiometric mixture of vanadium powder and iodine pieces was loaded in a silica tube and sealed under vacuum. Growth was performed over 3-4 days in a horizontal tube furnace, with the hot end held at 400 °C and the cold end at ambient temperature. High-resolution ARPES experiments were performed at Beamline 4.0.3

(MERLIN) of the Advanced Light Source using 30 - 128 eV linearly or circularly polarized photons in a vacuum better than 5×10^{-11} Torr. The total-energy resolution was 20 meV with an angular resolution $\Delta\theta$ of $\leq 0.2^\circ$.

Figure 2 shows the measured electronic band structure at $T = 264$ K using photon energy $h\nu = 76$ eV and out-of-plane linearly polarized light, within the setup in Figure 4e (detailed later). Measurements were done at 265 K to avoid charging of the sample. Despite the fact that this is well above the magnetic transition temperature reported for VI_3 (≈ 50 K¹⁴), previous ARPES measurements report no major differences in the band structure at 35 K and 300 K¹³. We calculate the curvature of the data in the energy direction (Figure 2 (a)), using the method elaborated in 15 . At the high symmetry direction $\text{K}-\Gamma-\text{K}$, we observe a non-dispersive band at the top of the conduction band (≈ 1 eV below the Fermi level) and dispersive bands at higher binding energies. A constant energy map at 4.5 eV below the Fermi energy (2(c)), reveals a six-fold symmetry, consistent with the known trigonal structure for VI_3 at room temperature. The superimposed blue hexagon corresponds to the first Brillouin zone, calculated using the parameters $a=b=6.89 \text{ \AA}^{-1}$ and $c=19.81 \text{ \AA}^{-1}$ reported in the literature from single crystal x-ray diffraction experiments^{14,16}. As in reference 13, we identify the flat band near the top of the valence band of V 3d character. As stated by Kundu et al, other V based vdW materials such as VSe_2 ¹⁷ and VTe_2 ¹⁸, show equally weakly dispersing V 3d-electron-derived bands. The attributed V 3d character of this band at ≈ 1 eV below the Fermi energy is also consistent with our photon energy dependent photoemission data. Following the work by Kundu et al., we compare the calculated photoemission crosssections^{19,20} to energy distribution curves (EDC) for different photon energies (See Supplementary Materials), where we verify that V 3d-electron derived bands show a stronger intensity for certain photon energies (vs I 5p bands) as listed in 19 and 20.

We explored the effect of electron doping by performing a gradual in-situ potassium (K) deposition. Doping created an interesting spectral weight redistribution, as shown in Figure 3. As we doped with electrons, weight grew significantly at the V 3d identified band, while increasing at lower amounts or staying the same at higher binding energies. The amount of K dosed on the surface of VI_3 had a very weak impact on the spectral weight at deep binding energies (below 7 eV). In contrast, the top of the valence band showed in addition to an important grow in weight, a noticeable broadening and a modest shift to higher binding

energies as more K was deposited. This behavior is in sharp contrast with the effect of in-situ doping on semiconductors or even Mott insulators, where the K-donated electrons usually trigger a rigid shift of the valence bands toward higher binding energies with no spectral weight redistribution. In those cases, an energy band gap can be estimated from the consequential shift of the chemical potential into the conduction band²¹. Here, the observed change of the band structure with doping suggests a non-conventional evolution of the VI₃ Mott state with doping.

Using different polarizations of the synchrotron light in ARPES is known to reveal hidden traits in the electronic band structure, or to help identifying the orbital character of materials' band manifolds²²⁻²⁵. As observed in Figure 4, in our setup (Beamline 4.0.3 at the ALS) the high energetic light is incident in the $k_y=0$ plane (65° relative to the analyzer lens), which breaks any geometrical symmetry about the crystal $k_x=0$ plane. As a consequence, there is no symmetry in the photoemission measured between $\pm k_x$ points for different light polarizations, and in contrast there is a generic geometrical dichroism (difference in the photoemission for two opposite light polarizations) above and below the $k_y = 0$ incident plane (at $\pm k_y$ for any k_x), provided that the crystal has also a symmetry above and below the $k_y = 0$ plane. In this study, we make use of linearly and circularly polarized light. In a first instance, we use out-of-plane \perp (or LH) and in-plane \parallel (or LV) light polarizations. In the case of \perp light, the electric field vector of the incident photons has a perpendicular component with respect to the sample surface, while for \parallel light, the electric field is always parallel to the sample surface (see Figure 4e). Figures 4a and b show VI₃ ARPES measured for both in-plane \parallel and out-of-plane \perp light polarizations in the K- Γ -K direction, as indicated in Figure 2c. We observe that different bands are enhanced with the two light polarizations. In particular, \perp light polarization reveals a stronger contribution from the band near 1 eV below the Fermi energy with respect to other bands at higher binding energies. This is summarized in Figure 4c, where the difference in ARPES intensity using the two polarizations (blue \perp , red \parallel) known as linear dichroism, is calculated. We have represented in Figure 4d the momentum-integrated energy distribution curves (EDCs) for the \perp (blue) and \parallel (red) polarizations, normalized by the incident photon flux. We observe that the intensity of the band near 1 eV below the Fermi energy is appreciably reduced for the \parallel with respect to the \perp light polarization (by 21%). Our linear dichroism data shows therefore that the V-3d-electron-derived bands are particularly sensitive to \perp light polarization,

indicating that their orbitals are ordered mainly orthogonal to the sample surface, while bands at higher binding energies (associated to I 5p orbitals¹³) seem to be ordered mainly parallel to the sample surface (ab plane). The former bands host the t_{2g} orbitals that set the Mott insulating behavior in VI_3 as well as its magnetic properties. As mentioned in the introduction, two possible scenarios explain the electronic properties of VI_3 . One in which V d^2 electrons occupy the $|e'_{\pm}\rangle$ orbitals and another where the V d^2 electrons occupy the $|a_{1g}\rangle$ and $|e'_{-}\rangle$ orbitals. The real part of the $|e'_{\pm}\rangle$ orbitals can be represented in coordinates with the z axis along the [111] axes of the crystal ($|e'_{g1}\rangle$ and $|e'_{g2}\rangle$), where they lie in the x-y plane (with some tilting of $|e'_{g2}\rangle$ with respect to $|e'_{g1}\rangle$)²

$$|e'_{g1}\rangle = \frac{1}{\sqrt{3}}(\sqrt{2}(x^2 - y^2) - xz)$$

$$|e'_{g2}\rangle = \frac{1}{\sqrt{3}}(\sqrt{2}xy + yz).$$

On the other hand, the $|a_{1g}\rangle$ orbitals are real and oriented parallel to the z direction^{2,3},

$$|a_{1g}\rangle \approx 3z^2 - r^2.$$

The measured linear dichroism for the V 3d bands points towards orbitals oriented mostly out-of-plane and therefore to a preferred $a_{1g}^1 e_{\pm}^1$ ground state for VI_3 , instead of a $e_{\pm}^2 a_{1g}^0$ ground state where orbitals are expected to be fully on-plane.

In order to explore further the orbital character details of the VI_3 valence bands, we studied the ARPES circular dichroism in the photoelectron angular distribution (CDAD), by using left- (LC) and right- hand (RC) circularly polarized light. In general, CDAD can be observed in an experimental geometry with a handedness. CDAD is absent when the geometry is such that a symmetry operation that transforms right- into left-circularly polarized light leaves the momentum vector of the photoelectrons \mathbf{k} unaffected²⁶. This is the case of the $k_y = 0$ plane (in blue in Figure 5d), that transforms right into left circularly polarized light without affecting \mathbf{k} , parallel to \hat{n} , the normal to the sample. There is therefore zero CDAD for $k_y=0$. On the other hand on the detector plane (yellow plane in Figure 5d), a reversal of the light polarization changes the sign of the y component of \mathbf{k} , leading to a non-zero CDAD. In our data, the CDAD is zero at Γ , as observed in Figure 5c. The handedness of the experimental setup combined with the symmetry of the orbitals making up the band structure of VI_3 , result in an CDAD intensity with opposite sign when crossing Γ along k_y . Despite the fact that CDAD has been argued to be a final state effect^{26,27},

it is worth it to point out that here, the V 3d identified bands exhibit the same CDAD polarization, while bands at higher binding energies (below 1 eV) show a switching of the CDAD. This is in contrast with the linear dichroism, that shows the same important LV light polarization effect at binding energies below 1 eV.

Finally, we study the photon energy dependence of VI_3 ARPES. Figure 6 shows data taken along the $\text{K}-\Gamma-\text{K}$ direction with \perp photons in a photon energy range of 60-120 eV. The top of the VI_3 valence band stays at about the same energy position for different photon energies, indicating a very weak band dispersion along the k_z direction, characteristic of layered materials with no interacting layers.

In summary, using different light polarizations, our ARPES study on the vdW Mott ferromagnet VI_3 points towards a ground state where V d^2 electrons occupy the $|a_{1g}\rangle$ and half fill the $|e'_{\pm}\rangle$ state. Circularly polarized light shows the same dichroism (CDAD) for the identified V 3d states while alternating CDAD at higher binding energies, indicating the same orbital character of the V 3d bands near the top of the conduction band. Our photon energy dependent measurements confirm the layer character of VI_3 , with weakly interacting layers. Most importantly, our measurements put in evidence in an indirect way the importance of spin-orbit coupling in this vdW ferromagnet, that leads to the $a_{1g}^1 e_{\pm}^1$ state, expected to be metallic unless spin-orbit coupling and electronic correlations are active and open a Mott band gap. As detailed in the introduction, spin orbit coupling in VI_3 plays indeed an essential role in the observed perpendicular magnetic anisotropy, essential for electronic applications.

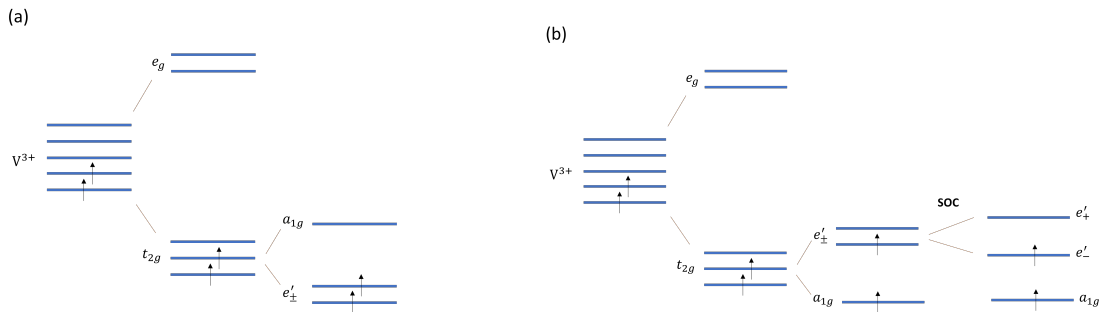


FIG. 1. **Splitting of the d energy levels in V $3d^2$** in the $e_{\pm}^2 a_{1g}^0$ (a) and $a_{1g}^1 e_{\pm}^1$ (b) configurations, the last one with active SOC coupling

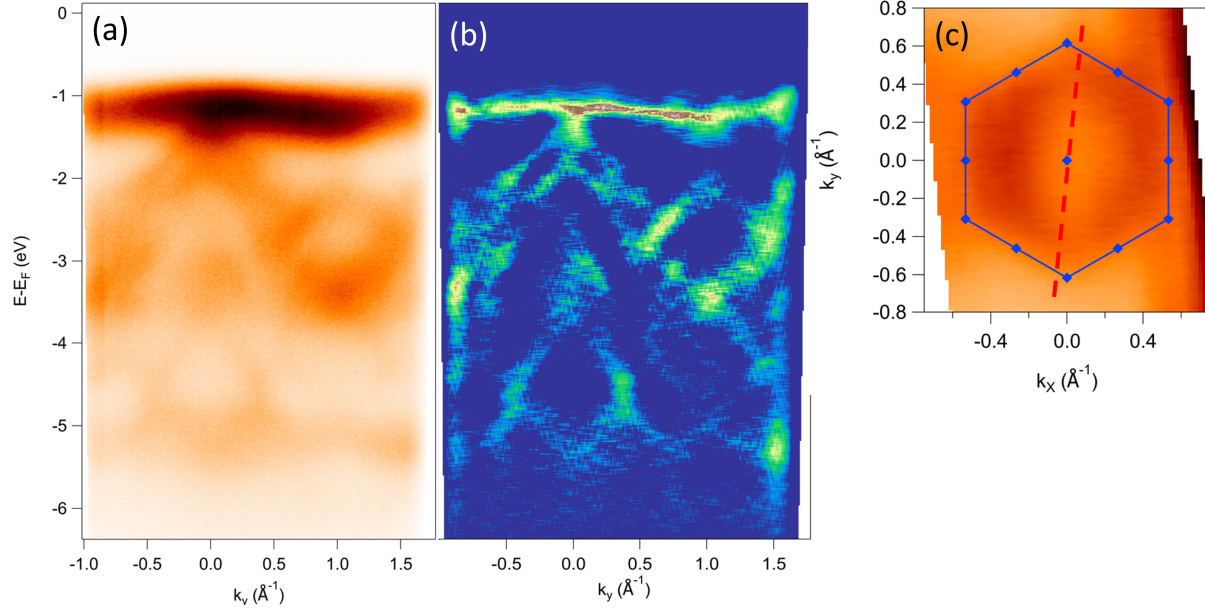


FIG. 2. **VI₃ band structure** a) ARPES measured along a line close to the high symmetry direction K- Γ -K, as indicated by the pointed line in (c). (b) Curvature of the measured electronic band structure shown in (a). (c) Constant energy map taken at 4.5 eV below the Fermi energy. The blue hexagon indicates the first Brillouin zone.

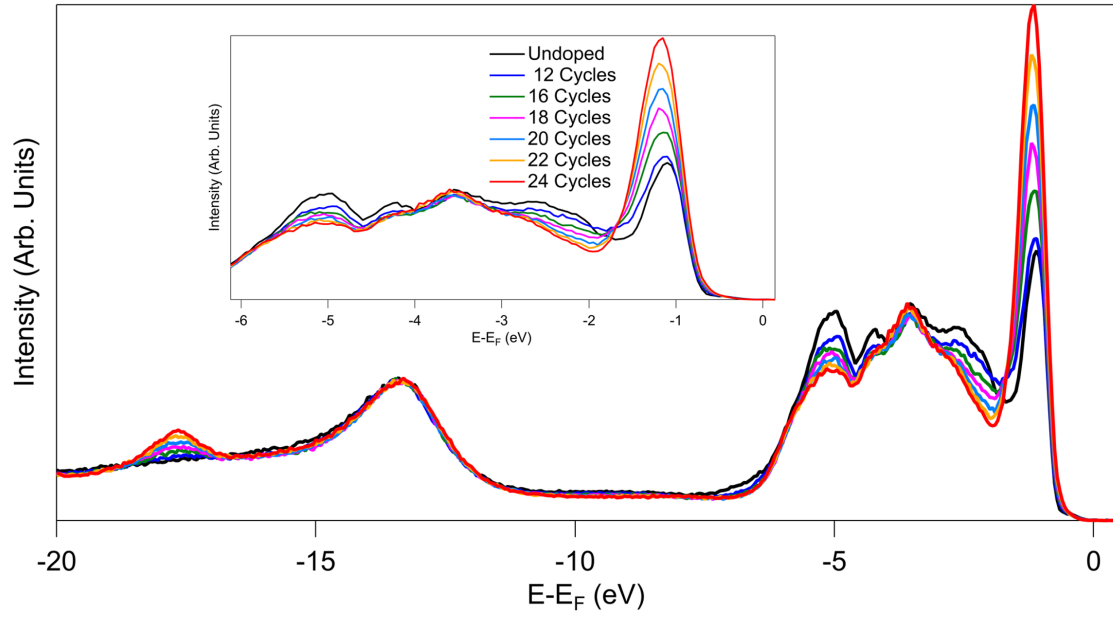


FIG. 3. **Effect of in-situ K doping** Momentum-integrated energy distribution curves after multiple cycles of doping. Each cycle corresponds to 4.0 Amps applied to a K effusion cell during 1 minute. The red curve corresponds to no-doping, the dark blue curve is the highest K doping. The K associated peak (17.5 eV) grows through the doping cycles.

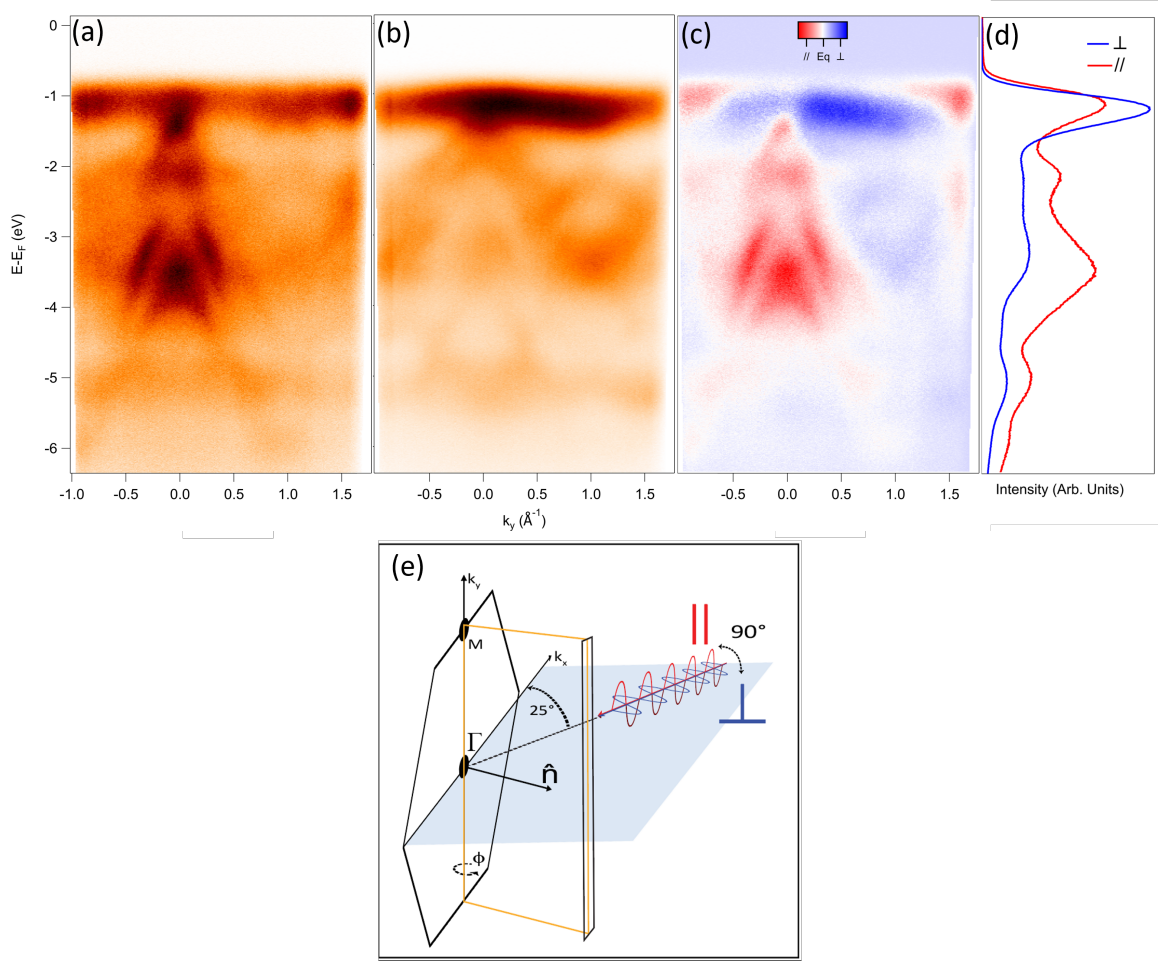


FIG. 4. **Linear polarization dependent VI_3 band structure** using in-plane (a) and out of plane (b) light polarization. (c) Linear dichroism calculated from the difference in intensities in figures (a) and (b). (d) Momentum integrated Energy Distribution Curve mEDCs for out-of-plane light polarization (blue curve) and in-plane light polarization (red curve). (e) Schematics of the experimental setup showing incident photons polarized in-plane \parallel (red) and out-of-plane \perp (blue). Photons are incident on the blue plane 25° with respect to the surface of the sample (65° with respect to the normal of the sample \hat{n}). The rectangle in black represents the detector slit and in orange the detector plane. M and Γ label high symmetry points of the first Brillouin zone and ϕ the polar angle that allows to reach different k_x . Data presented in the figure is taken at normal emission, $\phi = 0$.

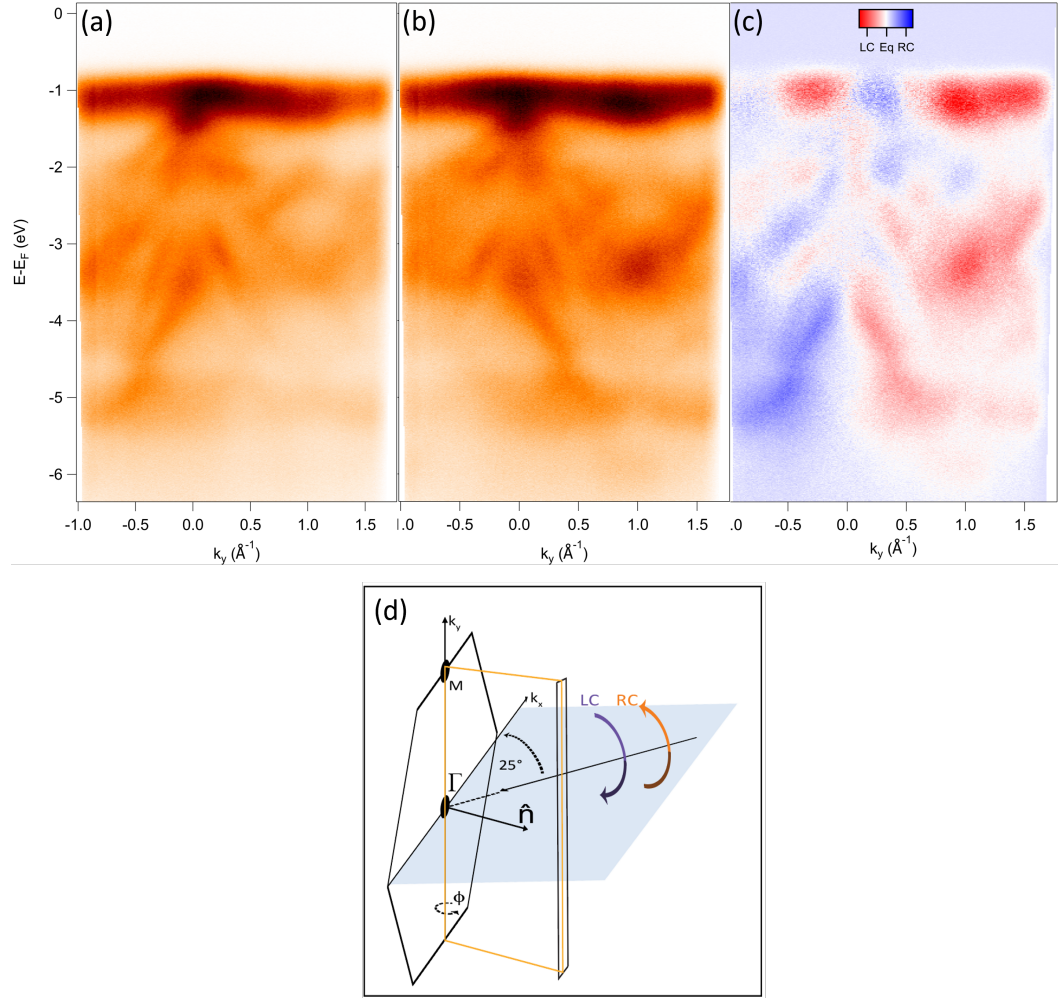


FIG. 5. **Circular dichroism of VI_3 ARPES** a) VI_3 ARPES using left-hand circularly (LC) (a) and right-hand circularly polarized (RC) light (b) along the $\text{K}-\Gamma-\text{K}$ direction. (c) Circular dichroism calculated using (a) and (b). (d) Schematics of the experimental setup as in figure 4e showing incident photons right-hand (red) and left-hand (blue) circularly polarized.

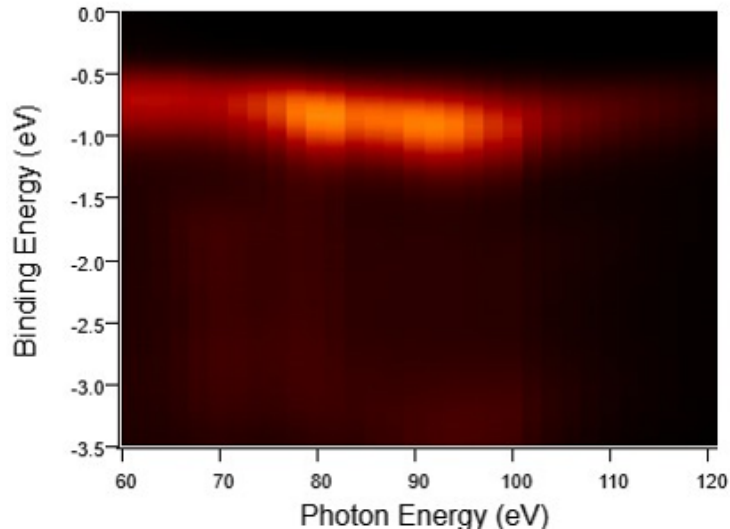


FIG. 6. **Photon energy dependence of the photoemission** along the K- Γ -K direction in the photon energy range 60 - 120 eV.

ACKNOWLEDGMENTS

The primary funding of this work was provided by the U.S. Department of Energy, Office of Science, Office of Basic Energy Sciences under contract DE-SC0018154. The crystal growth work conducted at Princeton University was supported by the NSF-sponsored PARADIGM program centered at Cornell University, grant DMR-1539918 We would like to acknowledge invaluable advice from Jonathan Denlinger from the Advanced Light Source at LBL as well as important discussions with Peng Zhang and calculations from Elton J. G. Santos, Benjamin Carpenter and Ignacio Martin Allati.

REFERENCES

- ¹Z. Lin, B. Huang, K. Hwangbo, Q. Jiang, Q. Zhang, Z. Liu, Z. Fei, H. Lv, A. Millis, M. McGuire, D. Xiao, J.-H. Chu, and X. Xu, “Magnetism and its structural coupling effects in 2d ising ferromagnetic insulator vi3,” *Nano Letters* **21**, 9180–9186 (2021), pMID: 34724786, <https://doi.org/10.1021/acs.nanolett.1c03027>.
- ²D. I. Khomskii, *Transition Metal Compounds* (Cambridge University Press, 2014).
- ³T. P. T. Nguyen, K. Yamauchi, T. Oguchi, D. Amoroso, and S. Picozzi, “Electric-field

- tuning of the magnetic properties of bilayer vi_3 : A first-principles study,” *Phys. Rev. B* **104**, 014414 (2021).
- ⁴Y.-P. Wang and M.-Q. Long, “Electronic and magnetic properties of van der waals ferromagnetic semiconductor vi_3 ,” *Phys. Rev. B* **101**, 024411 (2020).
- ⁵C. Huang, F. Wu, S. Yu, P. Jena, and E. Kan, “Discovery of twin orbital-order phases in ferromagnetic semiconducting vi_3 monolayer,” *Phys. Chem. Chem. Phys.* **22**, 512–517 (2020).
- ⁶K. Yang, F. Fan, H. Wang, D. I. Khomskii, and H. Wu, “ vi_3 : A two-dimensional ising ferromagnet,” *Phys. Rev. B* **101**, 100402 (2020).
- ⁷N. D. Mermin and H. Wagner, “Absence of ferromagnetism or antiferromagnetism in one- or two-dimensional isotropic heisenberg models,” *Phys. Rev. Lett.* **17**, 1133–1136 (1966).
- ⁸B. Huang, G. Clark, E. Navarro-Moratalla, D. R. Klein, R. Cheng, K. L. Seyler, D. Zhong, E. Schmidgall, M. A. McGuire, D. H. Cobden, W. Yao, D. Xiao, P. Jarillo-Herrero, and X. Xu, “Layer-dependent ferromagnetism in a van der waals crystal down to the monolayer limit,” *Nature* **546**, 270–273 (2017).
- ⁹C. Gong, L. Li, Z. Li, H. Ji, A. Stern, Y. Xia, T. Cao, W. Bao, C. Wang, Y. Wang, Z. Q. Qiu, R. J. Cava, S. G. Louie, J. Xia, and X. Zhang, “Discovery of intrinsic ferromagnetism in two-dimensional van der waals crystals,” *Nature* **546**, 265–296 (2017).
- ¹⁰J. L. Lado and J. Fernández-Rossier, “On the origin of magnetic anisotropy in two dimensional cri_3 ,” *2D Materials* **4**, 035002 (2017).
- ¹¹D.-H. Kim, K. Kim, K.-T. Ko, J. Seo, J. S. Kim, T.-H. Jang, Y. Kim, J.-Y. Kim, S.-W. Cheong, and J.-H. Park, “Giant magnetic anisotropy induced by ligand ls coupling in layered cr compounds,” *Phys. Rev. Lett.* **122**, 207201 (2019).
- ¹²A. Koriki, M. Míšek, J. Pospíšil, M. Kratochvílová, K. Carva, J. Prokleška, P. Doležal, J. Kaštil, S. Son, J.-G. Park, and V. Sechovský, “Magnetic anisotropy in the van der waals ferromagnet Vi_3 ,” *Phys. Rev. B* **103**, 174401 (2021).
- ¹³A. K. Kundu, Y. Liu, C. Petrovic, and T. Valla, “Valence band electronic structure of the van der waals ferromagnetic insulators: Vi_3 and cri_3 ,” *Scientific Report* **10** (2020), [10.1038/s41598-020-72487-5](https://doi.org/10.1038/s41598-020-72487-5).
- ¹⁴T. Kong, K. Stolze, E. I. Timmons, J. Tao, D. Ni, S. Guo, Z. Yang, R. Prozorov, and R. J. Cava, “ Vi_3 —a new layered ferromagnetic semiconductor,” *Advanced Materials* **31**, 1808074 (2019), <https://onlinelibrary.wiley.com/doi/pdf/10.1002/adma.201808074>.

- ¹⁵P. Zhang, P. Richard, T. Qian, Y.-M. Xu, X. Dai, and H. Ding, “A precise method for visualizing dispersive features in image plots,” *Review of Scientific Instruments* **82**, 043712 (2011), <https://doi.org/10.1063/1.3585113>.
- ¹⁶P. Doležal, M. Kratochvílová, V. Holý, P. Čermák, V. Sechovský, M. Dušek, M. Míšek, T. Chakraborty, Y. Noda, S. Son, and J.-G. Park, “Crystal structures and phase transitions of the van der waals ferromagnet Vi_3 ,” *Phys. Rev. Materials* **3**, 121401 (2019).
- ¹⁷J. Feng, D. Biswas, A. Rajan, M. D. Watson, F. Mazzola, O. J. Clark, K. Underwood, I. Marković, M. McLaren, A. Hunter, D. M. Burn, L. B. Duffy, S. Barua, G. Balakrishnan, F. Bertran, P. Le Fèvre, T. K. Kim, G. van der Laan, T. Hesjedal, P. Wahl, and P. D. C. King, “Electronic structure and enhanced charge-density wave order of monolayer vse_2 ,” *Nano Letters* **18**, 4493–4499 (2018), pMID: 29912565, <https://doi.org/10.1021/acs.nanolett.8b01649>.
- ¹⁸Y. Wang, J. Ren, J. Li, Y. Wang, H. Peng, P. Yu, W. Duan, and S. Zhou, “Evidence of charge density wave with anisotropic gap in a monolayer vte_2 film,” *Phys. Rev. B* **100**, 241404 (2019).
- ¹⁹D. E. Parry, “Atomic calculation of photoionization cross-sections and asymmetry parameters j.-j. yeh, published by gordon and breach, langhorne pa, 1993 isbn 2-88124-585-4 price \$125 (*\$65), £82 (*£42), ecu 104 (*ecu 54) (*special price for individuals who order direct from the publisher),” *Rapid Communications in Mass Spectrometry* **8**, 579–579 (1994), <https://analyticalsciencejournals.onlinelibrary.wiley.com/doi/pdf/10.1002/rcm.1290080716>.
- ²⁰J. Yeh and I. Lindau, “Atomic subshell photoionization cross sections and asymmetry parameters: 1 $leq z leq 103$,” *Atomic Data and Nuclear Data Tables* **32**, 1–155 (1985).
- ²¹R. Comin, G. Levy, B. Ludbrook, Z.-H. Zhu, C. N. Veenstra, J. A. Rosen, Y. Singh, P. Gegenwart, D. Stricker, J. N. Hancock, D. van der Marel, I. S. Elfimov, and A. Damascelli, “ na_2iro_3 as a novel relativistic mott insulator with a 340-mev gap,” *Phys. Rev. Lett.* **109**, 266406 (2012).
- ²²D. W. Latzke, C. Ojeda-Aristizabal, J. D. Denlinger, R. Reno, A. Zettl, and A. Lanzara, “Orbital character effects in the photon energy and polarization dependence of pure c60 photoemission,” *ACS Nano* **13**, 12710–12718 (2019), pMID: 31638764, <https://doi.org/10.1021/acsnano.9b04536>.
- ²³X.-P. Wang, P. Richard, Y.-B. Huang, H. Miao, L. Cevey, N. Xu, Y.-J. Sun, T. Qian, Y.-M. Xu, M. Shi, J.-P. Hu, X. Dai, and H. Ding, “Orbital characters determined from

- fermi surface intensity patterns using angle-resolved photoemission spectroscopy,” *Phys. Rev. B* **85**, 214518 (2012).
- ²⁴K. Volckaert, H. Rostami, D. Biswas, I. Marković, F. Andreatta, C. E. Sanders, P. Majchrzak, C. Cacho, R. T. Chapman, A. Wyatt, E. Springate, D. Lizzit, L. Bignardi, S. Lizzit, S. K. Mahatha, M. Bianchi, N. Lanata, P. D. C. King, J. A. Miwa, A. V. Balatsky, P. Hofmann, and S. Ulstrup, “Momentum-resolved linear dichroism in bilayer mos_2 ,” *Phys. Rev. B* **100**, 241406 (2019).
- ²⁵Y. Cao, J. A. Waugh, X.-W. Zhang, J.-W. Luo, Q. Wang, T. J. Reber, S. K. Mo, Z. Xu, A. Yang, J. Schneeloch, G. D. Gu, M. Brahlek, N. Bansal, S. Oh, A. Zunger, and D. S. Dessau, “Mapping the orbital wavefunction of the surface states in three-dimensional topological insulators mos_2 ,” *Nat. Phys.* **9**, 499 (2013).
- ²⁶M. R. Scholz, J. Sánchez-Barriga, J. Braun, D. Marchenko, A. Varykhalov, M. Lindroos, Y. J. Wang, H. Lin, A. Bansil, J. Minár, H. Ebert, A. Volykhov, L. V. Yashina, and O. Rader, “Reversal of the circular dichroism in angle-resolved photoemission from bi_2te_3 ,” *Phys. Rev. Lett.* **110**, 216801 (2013).
- ²⁷C. Bigi, F. Mazzola, J. Fujii, I. Vobornik, G. Panaccione, and G. Rossi, “Measuring spin-polarized electronic states of quantum materials: $2h - \text{nbse}_2$,” *Phys. Rev. B* **103**, 245142 (2021).

SUPPLEMENTARY MATERIALS

I. PHOTON ENERGY DEPENDENCE OF ENERGY DISTRIBUTION CURVES COMPARED TO CALCULATED PHOTOIONIZATION CROSS SECTIONS

The contrast of energy distribution curves at different photon energies (Figure 7) with the calculated atomic subshell photoionization cross sections for the V 3d and I 5p related states as a function of photon energy^{19,20}, supports our identification of the flat band near the top of the valence band as V 3d electron-derived. At $h\nu = 60$ eV, the observed intensity at 1.2 eV below the Fermi energy (that we identify as V 3d derived states) is larger compared to the observed intensity at higher binding energies (below 1.5 eV) that we identify as I 5p derived states. This is consistent with the calculated cross sections for V 3d and I 5p related states at $h\nu=60$ eV. In the same way, at $h\nu = 110$ eV, the observed intensity at 1.2 eV below the Fermi energy is comparable to the observed intensity at higher binding energies (below 1.5 eV) which is also consistent with the calculated cross sections for V 3d and I 5p related states at $h\nu=110$ eV.

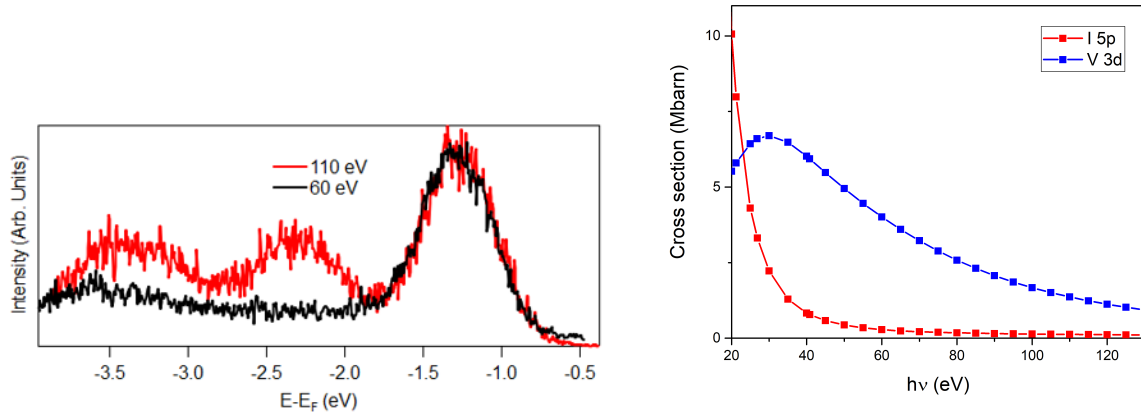


FIG. 7. **Supplementary materials** Left: Energy distribution curves at $k_y=1.1\text{\AA}^{-1}$ for photon energies $h\nu= 60$ eV (black) and 110 eV (red). Right: Calculated photoionization cross sections for V 3d (blue) and I 5p (red) related states from 19 and 20.